# Modeling of Plain Weave Fabric Composite Geometry

J. L. KUHN AND P. G. CHARALAMBIDES
*Department of Mechanical Engineering*
*The University of Maryland Baltimore County*
*Baltimore, MD 21228-5398*

(Received August 26, 1997)
(Revised July 19, 1998)

**ABSTRACT:** Woven unit-cell geometry functions are presented for a balanced plain weave fabric composite. Geometry models for polymer and ceramic matrix woven systems are developed. For polymer matrix woven systems, the space between bundles is fully occupied by the inter-bundle matrix phase which is modeled as a porous elastically isotropic medium. On the other hand, the woven unit-cell geometry model for ceramic matrix systems allows for the presence of both disperse porosity as well as large scale voids within the interbundle matrix region as needed to simulate the complex microstructure resulting from the Chemical Vapor Infiltration (CVI) processing technique. The geometry models take into account the existence of space between tows, the undulation of the tows, and the actual tow cross-sectional shape. Both the warp and transverse tows are modeled using piecewise continuous functions throughout the unit-cell domain. Equal accuracy in both the warp and fill directions, as required for biaxial and in-plane shear loading studies, is built into the geometry surface functions. The effects of the unit-cell geometry on the matrix and tow volume fractions for both the PMC and CMC systems are explored. Three-dimensional finite element meshes developed using these new mathematical geometry models are presented for both the porous matrix and matrix layer models.

## 1. INTRODUCTION

WOVEN FABRIC COMPOSITE materials have found widespread structural application in the last decade due to several attractive characteristics and the emergence of improved fabrication techniques. Consequently, there has been increasing interest in models to predict the mechanical behavior of this class of composite material. However, these materials possess highly complex microstructures which result in equally complex mechanical response. Unlike traditional



0021-9983/99/03 0188–33 $10.00/0

laminated composites, woven composites do not exhibit a uniform distribution of microstrain under a uniform remotely applied load. This non-uniform behavior is a key element of the mechanics of woven composite materials, and is a direct result of the complex geometry and microstructure of the woven fabric cross-section. The focus of this work is to present higher order geometry surface functions that are at the same time relatively compact and suitable for woven composite microstrain prediction by various techniques.

The most common approach to modeling the geometry of a woven composite ply has been to break the plane of the woven unit-cell into sub-regions and treat each sub-region as a traditional cross-ply laminate. Initially an approximate one-dimensional mosaic model that transformed the periodic tow shapes into heterogeneous rectangular regions was developed [1]. A tow undulation model was then developed by taking the limit of each heterogeneous zone size going to zero [1]. The one-dimensional models were extended to two-dimensional models such as the bridging model [2], wherein the shapes of the tows were refined to closely approximate the actual woven morphology [3,4]. This technique was improved by Ganesh and Naik [5], but the resulting expressions for the tow geometry are rather complex and difficult to implement, especially in related numerical finite element studies. In each of the above models, the woven morphology is broken into sub-domains, resulting in discontinuities or other mismatches in actual tow geometry which in turn yield lengthy expressions for the effective elastic composite stiffnesses. Another drawback of the above models is that they yield non-unique effective elastic properties as a result of the non-unique woven geometry employed by the models [6]. Such complexities have allowed little progress to be made in the development of fundamental predictive mechanical models for either PMC or CMC CVI woven composites.

Other alternatives to modeling the woven composite geometry have also been pursued. For example, Dasgupta and Agarwal [7,8] successfully assembled semicircular profiles to model plain weave composites. However, their model includes a layer of pure matrix between the tows in the interlace region, which does not often appear in actual systems. Whitcomb [9] presented a three-dimensional finite element model of the plain weave fabric unit-cell geometry. The woven unit-cell geometry used in those finite element studies did not match existing analytical geometry models, and was applicable to only soft matrix composites due to the assumed elastic miss-match of the elements in the inter-bundle matrix regions. Whitcomb [9] did show that the microstrains in the woven unit-cell are non-uniform using the finite element method. In order to develop higher order analytical predictions of the distribution of micro-strains in agreement with those of the finite element method, an accurate description of the geometry is required.

R. A. Naik [10] and Cox and Flanagan [11] presented woven composite mechanics models using expressions that describe the centroidal axis of the tows in

conjunction with approximations of the cross-sectional shapes of the tows with assumptions of uniform distribution of microstrains or microstresses. Such models do not accurately describe the interface between tows. If accurately modeled in three dimensions, there would be regions of interference between the volume of the tows in some regions and gaps that do not exist in real systems in others. These details are critical for accurate prediction of the micro-strains in the woven unit-cell. Indeed, 3-D brick finite element models generally more closely resemble actual geometry, but require labor intensive development. In this work we propose functions that can be used for both the analytical models, and in automated 3-D finite element mesh generators.

A rigorous experimental study on the tow surface characteristics in plain weave polymer matrix fabric composites was conducted by Yurgartis et al. [12] with the aid of digital image analysis. The results presented a great deal of information regarding the three-dimensional and statistical nature of the tow shapes. A three-dimensional reconstruction of a single tow isolated from the surrounding matrix material and interlacing tows was presented. This view of the actual tow surface structure offers insight into the structure that can only be inferred from two-dimensional micrographs.

In this work, we take a very different approach from other researchers and treat the woven composite as a four layer laminated composite. Each layer has non-uniform thickness (which may be zero in some places) and non-uniform location of the individual layer mid-planes. This is done by writing spatially varying functions that describe the top and bottom surfaces of each layer. This approach yields compact expressions that are of higher accuracy than other models presented in the literature. Other relatively accurate geometry descriptions include those associated with 3-D finite element models [9,13] which are labor intensive to generate. Once developed the surface functions developed herein can be used in the classical lamination theory presented by Jones [14] to compute the effective laminate stiffnesses at each point in the plane of the composite. However, in the above reference, no emphasis is placed on laminates comprised of laminae with non-uniform thicknesses and positions, and care must be taken to ensure that the expressions properly account for the spatial variations.

In the following sections the geometry surface functions are developed for the plain weave fabric repeating unit-cell. Initially the characteristics of a plain weave fabric composite are studied. Subsequently, two geometry models are presented, each with similar woven tow construction but distinguished by different configurations of the inter-tow matrix. The first "porous matrix model" treats the matrix as a porous continuum fully occupying the inter-bundle region. The second "matrix layer model" is developed such that it accounts for the presence of large scale voids characteristic of CVI ceramic matrix composites.

## 2. PLAIN WEAVE FABRIC GEOMETRY SHAPE FUNCTIONS

As discussed above, in this work a new approach is employed in order to generate more compact unit-cell geometry functions which can accurately represent the microstructure exhibited by PMC and CVI CMC systems. The basis of the approach is to treat the woven unit-cell as a four layer system whose lamination morphology depends on position through piecewise continuous mathematical surface functions. Thus, each layer is defined by irregular top and bottom surfaces. In regions where a particular layer does not exist, the top and bottom surfaces are forced to coincide at the mid-plane, thus simulating a nonexistent layer with an auxiliary layer of zero thickness. The details of this approach are presented in Section 2.2 later in this paper. Before outlining the above layer-wise procedure, however, we shall first identify and quantify the various characteristics of the woven composites structure.

Woven composites differ from traditional composite laminates primarily in the complexity of their respective geometry. A woven composite laminate is comprised of individual stacked plies constructed of matrix impregnated bundles of fibers, also known as tows, woven together in a variety of patterns. Figure 1(a) illustrates a three layer woven composite laminate whereas Figure 1(b) illustrates a representative volume element of a single woven ply. The warp tows represent the strands in the longitudinal direction that comprise the underlying structure upon which the composite is built. The weft or filling tows, henceforth termed fill tows, are the strands interlaced in the transverse direction through the warp thus forming the woven fabric. As such, the $x$ axis of the coordinate system shown in Figure 1(c) is aligned with the longitudinal warp direction, $y$ is aligned with the transverse direction, and the

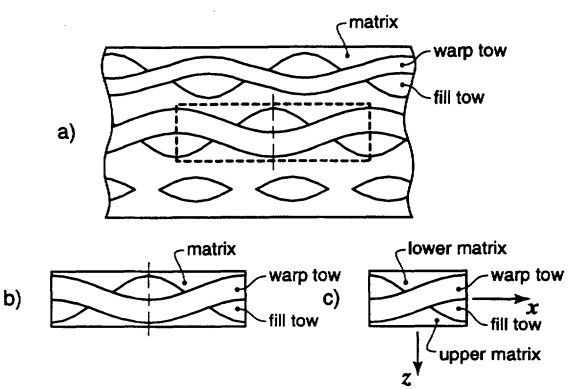


***Figure 1.*** *Plain weave fabric composite laminate morphology: (a) three woven plies stacked with random offsets between the undulation periodicity of each layer, (b) a representative volume element of a single woven ply and (c) the symmetric half of the woven unit-cell. The terminology upper and lower is adopted consistent with the downward positive z-direction.*

positive $z$ axis is chosen to point downward. The individual regions or cross-sections within the single ply shown in Figure 1(b) exhibit a lamination morphology similar to traditional cross-ply laminates. However, the thicknesses and positions of the tows within the ply vary in the $xy$ plane of the composite plate, and the tows represent individual strands as opposed to continuous layers in two dimensions.

The plain weave unit-cell geometry is comprised of bundles of untwisted fibers woven together in a simple alternating pattern. During the fabrication process fibers are collected together in a loose fashion to form tows which are interlaced prior to the introduction of the matrix. This yields a pliable mat that may be formed into complex shapes closely approximating the final desired geometry. Once formed into the final shape, the matrix material is then introduced with the aid of several techniques which vary substantially for polymer and ceramic matrix systems. Because the fiber bundles are woven together in a "dry" state, the form of the tows and the tow cross-sections conform to each other. As a result several key features are observed and a number of simplifying assumptions may be proposed.

## 2.1 Plain Weave Tow Geometry Characteristics

Close observations of micrographs presented by numerous researchers [3–5,7, 8,12,15–19] reveal the dominating geometry features of the woven mat. Because the micrographs represent cross-sectional views of the woven structures, some characteristics of the geometry must be inferred from the image data. The three key features of the plain weave architecture are the space between parallel tows, the shape of the tow undulation, and the tow cross-sectional shape. Based on observation of the micrographs a number of assumptions regarding these key features are developed. The periodic undulation of the tows are assumed to follow a sinusoidal form in the longitudinal direction and the fibers are assumed to be parallel to each other within each tow. The density of the fibers is assumed to be uniform, and the cross-sectional area of the tows is assumed to remain constant for different cross-sections along the length of the tow. In addition, the in-plane width of the tows is assumed to be constant along the longitudinal direction of the tows. The fibers and the slopes of the fibers are assumed to be continuous, and the fill and warp tows are assumed to be in full contact throughout the interlace region.

The geometry of the plain weave fabric composite can be characterized completely through consideration of the smallest representative volume element within a composite laminate. The dashed lines in Figure 1(a) outline the representative volume element isolated in Figure 1(b). For the purposes of analysis, the full unit-cell may be further reduced by utilizing the existing geometric symmetry. The resulting symmetric unit-cell is shown in Figure 1(c). The four components of the woven unit-cell are identified in Figure 1(c), where a coordinate system with its origin located in the mid-plane of the unit-cell and its $z$ axis pointing downward is defined. The isometric and top views of three different unit-cells shown in Figure

2 illustrate the main features of each unit-cell. The full unit-cell of Figure 2(a) may be reduced to the symmetric unit-cell of Figure 2(c) consistent with that of Figure 1. The unit-cell shown in Figure 2(b) is defined as the repeating unit-cell. While the repeating unit-cell is less conducive to analysis because of the lack of symmetry, the configuration may be aligned with the same coordinate system as that of the symmetric unit-cell and aid in identifying critical geometry characteristics.

As such, the repeating unit-cell is shown in Figure 3 in the absence of inter-tow matrix material. In the above figure, two warp tows are interlaced with two fill tows, and a coordinate system with the origin in the mid-plane and at the center of the space between tows is assigned for convenience. Key points are labeled to identify the structure of the woven mat and to aid in the discussion. Ganesh and Naik [5] defined the region of contact between the fill and warp tows labeled *cghd* in Figure 3 as the interlace region, and the space outside the interlace region, distinguished by a space between parallel tows in the plane of the composite, as the gap region. Here we retain the definition of the interlace region but modify the definition of the gap region to include only the area labeled *hmnj* in Figure 3. We identify the area labeled *dhje* as the fill bridge region, since in this region, the fill tow bridges the gap between the warp tows. Likewise, regions where the warp tows span the gap between fill tows are called warp bridge regions.

The geometry model developed herein is restricted to balanced non-hybrid plain weave fabric composites with an orthogonal weave pattern. As such, it is assumed that each of the four tows shown in Figure 3 are of exactly the same geometry. One can envision that tow #1 can be duplicated and rotated 90° about the $z$ axis to create tow #2. Likewise, tow #2 can be duplicated and rotated 90° about the $z$ axis to create tow #3, and in a similar manner tow #4 can be created from tow #3. Given the list of assumptions presented at the beginning of this section, the vertical thickness of the tows approach zero near the gap region, and maintain contact at points $h$, $m$, $n$, and $j$ in Figure 3. Because each of the tows are also assumed to take the same geometrical form, the edges $hm$, $mn$, $nj$, and $jh$ are straight and lie completely within the $xy$ plane.

The sections labeled A-A and B-B in Figure 3 are shown in Figure 4 in order to illustrate the key characteristics of the tow transverse and longitudinal cross-sections. The tow cross-sections are assumed to have a sinusoidal top and bottom profile that meet to form sharp points at the edges as shown in Figure 4. This is because the fibers within the tows are woven together prior to the introduction of the matrix material, allowing the fibers to shift such that the edges of the tows narrow to the thickness of only a few fibers. While at first glance the tow cross-sections appear to be symmetric about the axis extending from point to point (the dashed line labeled *rs* in Figure 4), close observation of actual micrographs reveals that there is a tendency for the profile constrained by contact with the adjacent tow in the interlace region to have a lower amplitude than the opposing unconstrained profile. While this feature may have little impact on the unit-cell volume fraction

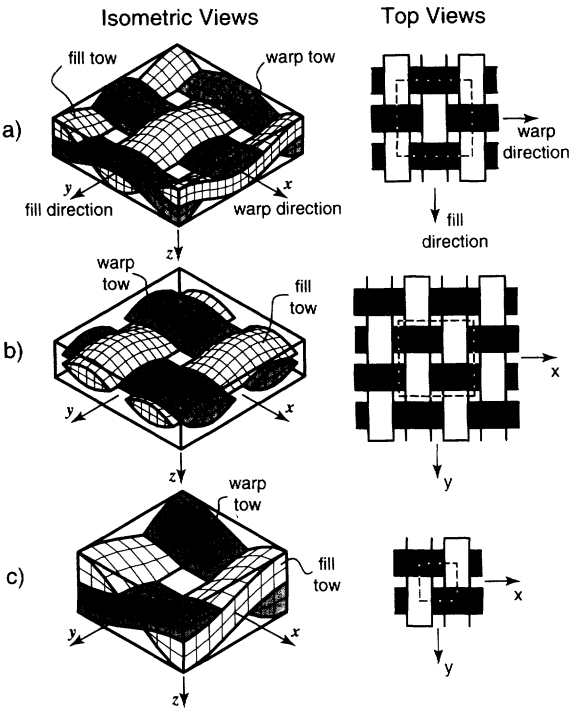


***Figure 2.*** *Three unit-cells of the plain weave fabric composite: (a) full repeating and geometrically symmetric unit-cell, (b) repeating unit-cell and (c) symmetric unit-cell.*

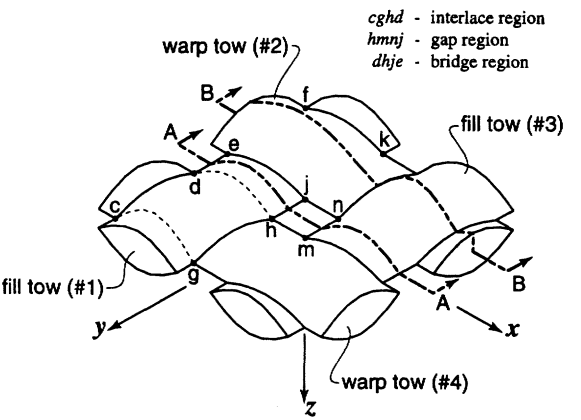


***Figure 3.*** *A plain weave mat consisting of two warp and two fill tows in the absence of inter-tow matrix. Sections A-A and B-B are shown in Figure 4, and a detailed view of fill tow #1 is shown in Figure 5. The interlace and gap regions are defined consistent with Ganesh and Naik [5], but modified with the addition of the bridge region.*

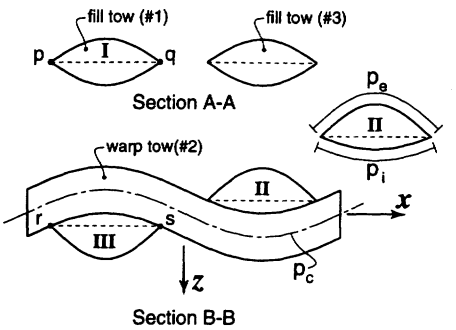


***Figure 4.*** *Plain weave mat sections from Figure 3. Section A-A is through the center of the bridge region, and section B-B is through the center of the interlace region. The curves labeled* $p_c$, $p_i$ *and* $p_e$ *represent the centroidal axis, internal edge and external edge profiles, respectively.*

and effective elastic property predictions, it is a critical aspect which results in full contact between tows, and plays an important role in the non-uniform distributions of strains within the unit-cell.

As shown in Figure 4, each tow is constrained from above on one side of the bridge region, and constrained from below on the other side of the bridge region. Consequently, the transverse tow cross-sections located in the center of the bridge region as shown in section A-A and labeled I in Figure 4, are assumed to be symmetric about the major axis labeled *pq*. The fill tow sections labeled II and III are constrained along the interior edge, labeled $p_i$, by warp tow #2 as shown in section B-B of Figure 4. The external edges of sections II and III are not constrained, and thus are assumed to have the sinusoidal shape with larger amplitude labeled $p_e$. This implies that the transverse cross-sections of the tows are not symmetric about the major axis in the interlace regions. Because the tows are all of self similar geometry, the shape of section III is a mirror image of section II reflected about the $x$ axis. The centroidal axis of warp tow #2 is assumed to follow the continuous sinusoidal profile labeled $p_c$. While all of the transverse cross-sections shown in Figure 4 are of fill tows, the same cross-sections may be identified in the warp tows. Likewise, the profile of the warp tow shown in Figure 4 is identical to that of the fill tows. The functions used to represent curves $p_c$, $p_e$ and $p_i$ are presented in Section 2.2.

A detailed view of the fill tow labeled #1 in Figure 3 is shown in Figure 5. The above figure shows the relationship between the tow transverse cross-sections and the undulation of the tow centroidal axis. The tow transverse cross-sections are assumed to be uniform through the length of the interlace regions. Hence, the cross-sections are of the form of section II in the interlace region labeled *cghd*, and section III in the interlace region labeled *ejkf*. The cross-sections in the domain of the bridge region are assumed to be constructed from a linear interpolation between sections II and III. Hence the transverse section at the center of the bridge

region will be symmetric and take the form of section I. The ends of the fill tow shown in Figure 5 lie at the center of bridge regions and take the form of section I.

Earlier we stated that the edges of the square *hmnj* shown in Figure 3 lie within the *xy* plane. These consequences result in the subtle discontinuities in the slope of the edge labeled *ghjk* in Figure 5. This edge, along with the longitudinal lines drawn on the surface of the tow, represents the shape of the fibers embedded in the tow. As such the assumption that the fibers are continuous is satisfied, but the assumption that the slopes of the fibers are continuous is not upheld with minor slope discontinuities predicted at points of changing cross-sectional shape, i.e., from type I to II, or I to III. The discontinuous slopes in the fibers diminish for fibers near to the center of the tow. The majority of the fibers in the volume of the tows have negligible discontinuities in the slope, and for the purposes of computing the material axes the fibers are assumed to be parallel to the tow centroidal curve, which is continuous. These discontinuities may be eliminated by relaxing one of the assumptions of the tow geometry. For example, in real systems, the tows may exhibit slight separation very near to the gap region, or the cross-sectional shapes may not take the form shown in Figure 5. Either case may allow the fibers to "straighten out." For simplicity and because the error is negligible, particularly for small aspect ratios and gap dimensions, the mathematical model will conform to the geometry presented in Figures 3–5.

The characteristics of the geometry outlined above do not take into account the matrix found outside of the tow geometry. This matrix, defined as the inter-tow matrix, may appear in different forms depending on the process used to fabricate the composite. In the following sections, mathematical models will be de-

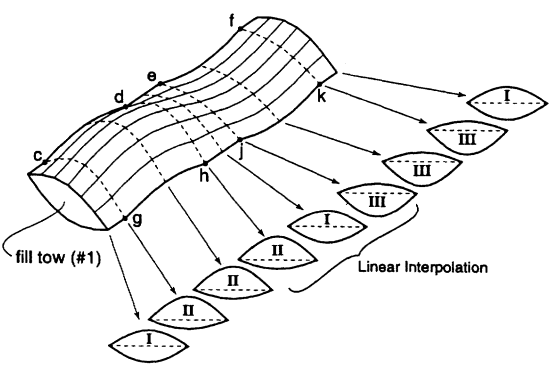


***Figure 5.*** *Detailed view of fill tow #1 from Figure 3. The lower case letter labels correspond with those of Figure 3, and the roman numeral cross-section labels correspond with those of Figure 4. The tow cross-sections in the interlace region are assumed to be constant, and the cross-sections in the bridge region are interpolated from the adjacent interlace regions. The longitudinal lines on the surface of the tow indicate expected fiber profiles.*

veloped to represent two different configurations of the inter-tow matrix. The characteristics of the geometry outlined above will be employed to develop mathematical expressions representing the top and bottom surfaces of each of the layers as mentioned earlier in this paper. First, the simpler porous matrix model is developed, and subsequently the differences incurred by the more complicated matrix layer model are presented.

## 2.2 Porous Matrix Model

The inter-tow matrix region of polymer matrix woven composites is typically fully dense or may contain dispersed porosity. As such, appropriate micromechanics models may be employed to represent the porous inter-tow material as an effectively fully dense continuum [15]. In accordance with the geometrical features discussed in the previous section and in accordance with a plain weave fabric composite with a potentially porous continuum matrix occupying all the space outside of the tows, the porous matrix model is defined and appropriate geometry parameters are introduced as shown in Figure 6. In this geometry model, the space between tows is taken into account, the continuity of the fibers is maintained, and the fiber orientation is allowed to vary along the length of the tow. The overall height of the ply is designated as $h$, and the maximum thickness of the individual tows are assigned the dimension $b$. The horizontal dimensions of $g$, $a$ and $l$ are assigned to the width of the gap and bridge regions, the half period of the tow undulation, and the overall width of the repeating unit-cell, respectively. The repeating unit-cell shown in the above figure reduces to the symmetric unit-cell for $l = a$. The notation $\theta_y^w$ is used to denote the out-of-plane rotation about the $y$ axis of the local material coordinates aligned with the fibers embedded within the warp tow. Likewise, the angle of out-of-plane rotation about the $x$ axis of the fill tow local material coordinates (not shown in Figure 6), is given by $\theta_x^f$.

Two adjacent side-views of the symmetric unit-cell are shown side by side in Figure 7. The shaded regions in left and right columns of Figure 7(a) represent the lower matrix layer, which is continuous with a non-uniform thickness. The term "lower" is defined consistent with the positive $z$ axis pointing downward. The two columns in Figure 7(b) show the fill tow layer, which is comprised of both the fill tows contained within the unit-cell. The layer is discontinuous with a region of zero thickness as shown on the left in Figure 7(b). The warp tow layer highlighted in row *c* of Figure 7 is self similar to the fill tow layer under a geometric transformation. As such the same discontinuity and zero thickness characteristics of the fill tow layer is also observed in the right side-view of the unit-cell, shown in Figure 7(c). The upper unit-cell matrix layer, defined consistent with the $z$ axis pointing downward is shown in Figure 7(d). This layer is shown to be self similar to the lower matrix layer, and is continuous with non-uniform thickness.

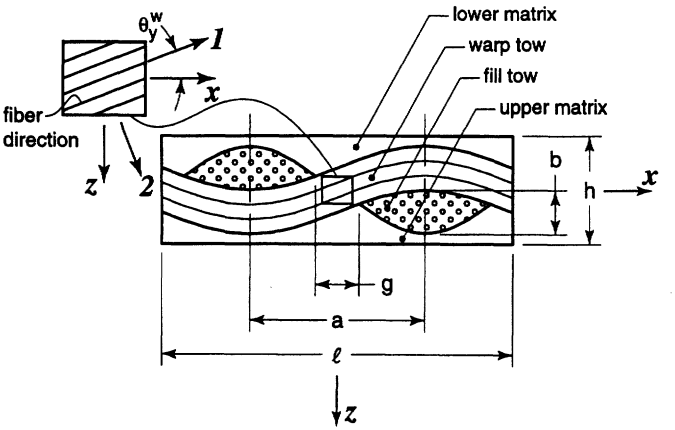


***Figure 6.*** *Plain weave fabric repeating unit-cell cross-sectional geometry and related parameters.*

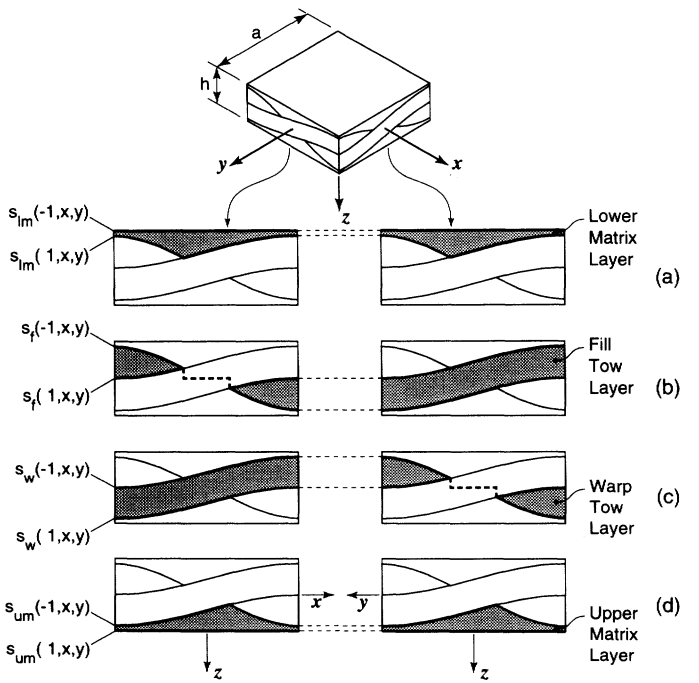


***Figure 7.*** *Side profiles of the four layers that constitute a single woven ply. The shaded portion of each row of figures illustrates two adjacent views of the: (a) lower matrix layer, (b) fill tow layer, (c) warp tow layer and (d) upper matrix layer. The labels on the left indicate the notation used to describe the distance from the mid-plane to the respective surface.*

The objective of this work is to write relatively compact functions to represent the top and bottom surfaces of the layers identified in the above figure. The thick solid and dashed lines bordering the shaded regions represent profiles of the surface functions along the side edges. In Figure 7, the notation $s_i(\eta,x,y)$ is used to denote each of the surfaces. In this notation the subscript $i$ indicates the layer. In this case the subscripts $lm$, $f$, $w$, and $um$ denote the lower matrix, fill, warp, and upper matrix layers respectively. The parameter $\eta$ is used to denote the top or bottom surface of the layer. A value of $-1$ indicates the bottom surface and $+1$ indicates the top surface consistent with positive $z$ pointing downward. With this approach a single function is used to describe the geometry of an individual layer. For example, the single function $s_{lm}(\eta,x,y)$ will be developed later in this paper for the lower matrix layer. In this function, if $-1$ is substituted for $\eta$ then the function describes the bottom surface, and if $+1$ is substituted for $\eta$ then the function describes the top surface.

While Figure 7 is an illustration of the plain weave architecture, the four layer designation may also be applied equally as well to other two-dimensional architectures such as the four- and eight-harness satin weaves. The non-uniform laminated plate theory can also be applied to more complex two-dimensional weaves such as the triaxial braided weave by including additional layers for each added tow direction.

The equation describing the profile of the warp tow centroidal axis, $p_c$ (see Figure 4), utilizing the above geometry parameters is

$$p_c(x) = -\sin\left(\frac{\pi x}{a}\right) \tag{1}$$

The above equation may be used to describe the centroidal axis of each of the tows by changing the sign and/or replacing the $x$ coordinate with the $y$ coordinate. The internal profile of the tow cross-section has the same form as the tow centroidal axis in order to maintain contact between the tows and for a point located at position $x$, it is given in terms of its absolute value $|x|$, as follows:

$$p_i(x) = \sin\left(\frac{\pi |x|}{a}\right) \tag{2}$$

The external profile of the tow cross-section is also sinusoidal in shape but the amplitude is modified in order to account for the gap region and account for the non-symmetry of the tow cross-section as follows:

$$p_e(x) = (1+\beta)\sin\left(\frac{\pi(|x|-g/2)}{(a-g)}\right) - \beta$$
$$\beta = \sin\left(\frac{\pi g}{2a}\right) \tag{3}$$

The above profiles may be employed to model the top surface of the tow shown in Figure 8(a) in the domain of $(-a/2) \le x \le (a/2)$ and $(g/2) \le y \le (a/2)$ by assembling them in a linear combination with the following discontinuous interpolation function as the coefficients

$$R(x) = \begin{cases} \dfrac{x}{g} + \dfrac{1}{2} & |x| < \dfrac{g}{2} \\ H(x) & \dfrac{g}{2} \le |x| \le a - \dfrac{g}{2} \\ \dfrac{(\text{sign}(x)a - x) + \dfrac{1}{2}}{g} & a - \dfrac{g}{2} \le |x| \le a \end{cases} \tag{4}$$

where $H(x)$, the heavy side step function, is given by

$$H(x) = \begin{cases} 0 & x < 0 \\ 1 & 0 \le x \end{cases} \tag{5}$$

and sign$(x)$ is the discontinuous sign function, defined as

$$\text{sign}(x) = \begin{cases} -1 & x < 0 \\ +1 & 0 \le x \end{cases} \tag{6}$$

The above auxiliary equations are shown in Figure 9.

In order to generate the top surface of the tow as shown in Figure 8(a), the appropriate form of Equation (1) is written to describe the centroidal axis of the tow, and the functions outlining the tow transverse profile are summed. The top surface of the tow in the interlace region in the $x > 0$ and $y > 0$ domain has the profile $p_i$, and the top surface in the other interlace region has the profile $p_e$. Thus $p_i$ is multiplied by the ramp function [Equation (4)] and summed with the centroidal axis profile. In the respective interlace region, the ramp function has a magnitude of 1, and as such, the profile is unaffected. In the bridging region the ramp function varies linearly from 1 to 0, which when reversed and multiplied by the other profile $p_e$ and summed, gives rise to a linear interpolation between $p_i$ and $p_e$ in the bridge region. Equations (1) through (4) are thus assembled to form the surface function of the top of the tow shown in Figure 8(a), resulting in

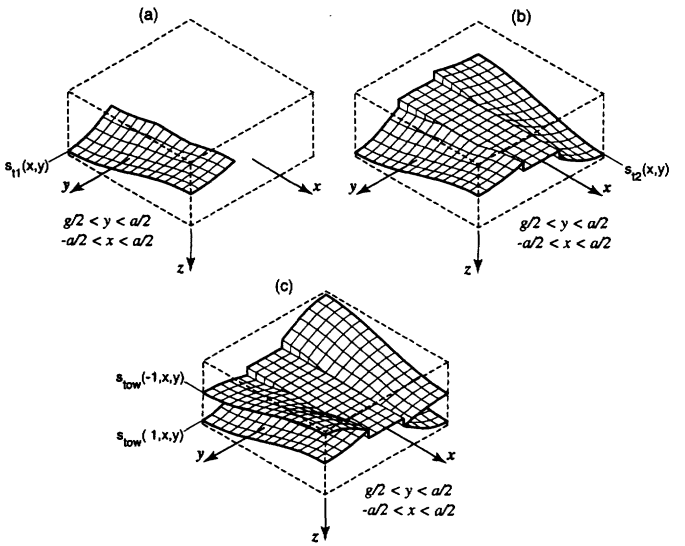


***Figure 8.*** *Surface plots of the functions describing the surfaces of the tow at each stage in the derivation. The dashed lines outline the domain of the symmetric unit-cell: (a) the top surface of a single tow, (b) the top surface of the entire tow layer and (c) the top and bottom surfaces of the tow layer.*

$$H(x) = \begin{cases} 0 & x < 0 \\ 1 & 0 \le x \end{cases}$$

$$\text{sign}(x) = \begin{cases} -1 & x < 0 \\ +1 & 0 \le x \end{cases}$$

$$R(x) = \begin{cases} \frac{x}{g} + \frac{1}{2} & |x| < \frac{g}{2} \\ H(x) & \frac{g}{2} \le |x| \le a - \frac{g}{2} \\ \frac{(\text{sign}(x)a - x)}{g} + \frac{1}{2} & a - \frac{g}{2} \le |x| \le a \end{cases}$$

$$F_H(x) = H\left(|x| - \frac{g}{2}\right) - H\left(|x| + \frac{g}{2} - a\right)$$

$$F_R(\eta, x, y) = R(\eta\, \text{sign}(y)\, x)$$

***Figure 9.*** *The auxiliary functions and their representative profiles used in constructing the geometry surface functions.*

$$s_{t1}(x,y) = \frac{b}{2}[p_c(x) + R(x)p_i(y) + R(-x)p_e(y)]$$
$$\text{in: } -a < x < a; \quad \frac{g}{2} < y < a - \frac{g}{2} \tag{7}$$

The above equation may be extended to describe the surface of the tow everywhere in the domain of the repeating unit-cell as follows:

$$s_{t2}(x,y) = \frac{b}{2} F_H(y)[\text{sign}(y)p_c(x)$$
$$+ R(\text{sign}(y)x)p_i(y) + R(-\text{sign}(y)x)p_e(y)] \tag{8}$$
$$in: -a < x < a; \quad -a < y < a$$

where the function $F_H(x)$ is used to force the surface height to zero in regions where the tow layer does not exist and is given by

$$F_H(x) = H\left(|x| - \frac{g}{2}\right) - H\left(|x| + \frac{g}{2} - a\right) \tag{9}$$

Here we recall that the parameter $\eta$ equaling $-1$ and $+1$ is used to represent the bottom and top surfaces of the tow, respectively. This notation is used to write the generalized tow surface function as

$$s_{tow}(\eta,x,y) = \frac{b}{2} F_H(y)[\text{sign}(y)p_c(x)$$
$$+ \eta F_R(\eta,x,y)p_i(y) + \eta F_R(-\eta,x,y)p_e(y)] \tag{10}$$
$$\text{in: } -a < x < a; \quad -a < y < a$$

where the $F_R(\eta,x,y)$ compound auxiliary function is

$$F_R(\eta,x,y) = R(\eta\,\text{sign}(y)x) \tag{11}$$

Each of the auxiliary equations employed above are shown in Figure 9. The warp and fill tow surface functions $s_w(\eta, x, y)$ and $s_f(\eta, x, y)$ in terms of the above generalized surface function are

$$s_w(\eta, x, y) = s_{tow}(\eta, x, y) \qquad \text{(warp tow)}$$
$$s_f(\eta, x, y) = -s_{tow}(-\eta, x, y) \qquad \text{( fill tow)} \tag{12}$$

which may be readily substituted into the generalized expressions for the woven composite laminate stiffnesses derived in Section 3. In this model, the fibers embedded in the tows are assumed to be parallel to the centroidal axes of the tows and, as such, the angles of rotation about the appropriate axis are given by

$$\theta_y^w = \text{atan}\left(-\frac{\pi b}{2}\,\text{sign}(y)\cos\left(\frac{\pi x}{a}\right)\right)$$
$$\theta_x^f = \text{atan}\left(\frac{\pi b}{2}\,\text{sign}(x)\cos\left(\frac{\pi y}{a}\right)\right) \tag{13}$$

The surface functions for the upper and lower matrix Equation (12) may be derived in terms of the tow surfaces in two steps. First the following surface function of the interface between the tows and the matrix is written

$$s_m(\eta, x, y) = \begin{cases} \text{MIN}(s_f(\eta, x, y), s_w(\eta, x, y)) & \eta = -1 \\ \text{MAX}(s_f(\eta, x, y), s_w(\eta, x, y)) & \eta = +1 \end{cases} \tag{14}$$

and the surface functions describing the top and bottom surfaces of the upper lower matrix layers are given by

$$s_{lm}(\eta, x, y) = \begin{cases} -\dfrac{h}{2} & \eta = -1 \\ s_m(-1, x, y) & \eta = +1 \end{cases} \quad \text{(lower matrix)}$$
$$s_{um}(\eta, x, y) = \begin{cases} s_m(+1, x, y) & \eta = -1 \\ +\dfrac{h}{2} & \eta = +1 \end{cases} \quad \text{(upper matrix)} \tag{15}$$

Each of the porous matrix model surface expressions given by Equations (12) and (15) are plotted for the symmetric unit-cell in Figure 10 for $b/a = 0.2$, $g/a = 0.286$, and $h/a = 0.45$. In the above figure, the definition of top and bottom is consistent with the positive $z$ axis pointing downward. As such, the fully visible grids in each figure are the bottom surfaces, and the partially hidden grids are the top surfaces, due to the orientation of the coordinate system. The functions shown in Figure 10 effectively represent the top and bottom surfaces of each of the four non-uniform layers that comprise the woven laminate. Both the fill and the warp tows are continuous along their length, and the gap region appears as a flat plate of thickness zero in each layer. The inter-tow matrix layers occupy the entire unit-cell

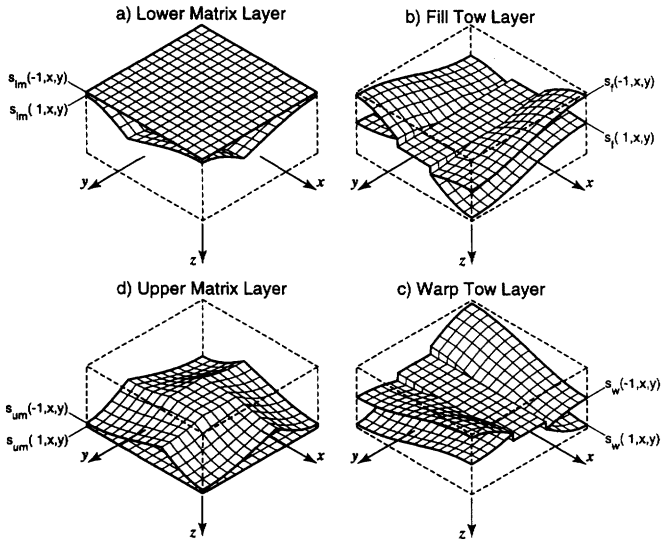


***Figure 10.*** *Plots of surface functions describing the top and bottom surfaces of each of the layers in the porous matrix model.*

space outside the tows. Seven cross-sections of the repeating unit-cell generated using Equations (12) and (15) are presented in Figure 11 for $b/a = 0.25$, $g/a = .025$, and $h/a = 0.55$. Sections numbered as 1, 2, 6 and 7 show that the tows remain continuous everywhere, while exhibiting small, almost not-detectable, slope discontinuities. Sections 1 and 2 are located within the interlace region, and section 3 is along the edge of the interlace region. In these three sections the tow transverse cross-sections appear to have the same shape. This is also true for sections 5, 6, and 7. Section 4 passes through the center of the bridging and gap regions, and as expected is shown to be symmetric about its respective major axis.

## 2.3 Matrix Layer Model

Ceramic matrix woven composites fabricated via the chemical vapor infiltration technique are characterized by macroscopic voids in the matrix between tows [15,20]. Figure 12(a) depicts a three-ply woven composite laminate, wherein the shaded regions represent voids not filled during fabrication. As in the case of the porous matrix model, the full unit-cell of a single layer is distinguished by dashed lines and isolated in Figure 12(b). The full unit-cell is reduced to the symmetric unit-cell shown in Figure 12(c), an appropriate coordinate system with $z$ pointing downward is assigned, and the four layers comprising a single plain weave fabric ply are identified. The inter-tow matrix appears as a thin layer with spatially vary-

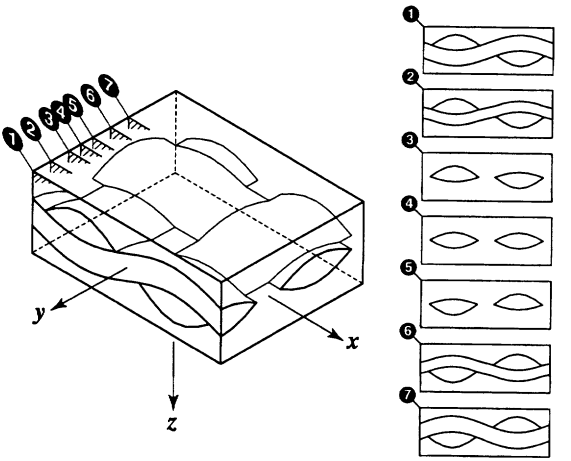


***Figure 11.*** *Plots of several cross-sectional areas generated using the porous matrix model developed herein. The cross-sections generated by these surface functions are identical in the transverse direction.*

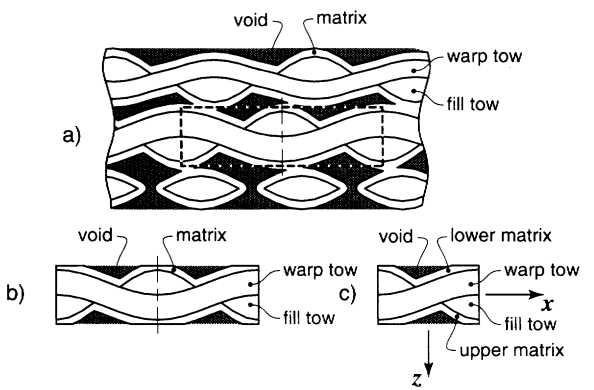


***Figure 12.*** *A schematic representation of a plain weave fabric laminated composite fabricated by the chemical vapor infiltration technique: (a) three woven layers stacked to form a composite laminate, with the full unit-cell outlined by the dashed lines. The plane of the view shown lies between warp tows in the bottom ply, illustrating that the voids may extend through the thickness of a single woven ply in the gap regions, (b) the full unit-cell isolated from the three layer system and (c) the symmetric unit-cell with the defined coordinate system and structural features labeled.*

ing thickness due to the presence of the macroscopic voids. The generality of the non-uniform composite laminate theory presented earlier allows this matrix to be treated as layers as in the case of the porous matrix model. All that is required is a mathematical description of the top and bottom surfaces of the matrix layers. This model is designated the matrix layer model to distinguish it from that of the previous section.

Each of the four layers of the matrix layer model are highlighted in Figure 13. The fill and warp tow layers shown in Figures 13(b) and 13(c), respectively are identical to those of the porous matrix model, and as such are described geometrically by the same surface expressions given by Equation (12). The lower and upper matrix layers shown in Figures 13(a) and 13(d) are distinguished from those of the porous matrix model by the non-uniform external surfaces and the presence of a hole in the center of the unit-cell. An additional geometry parameter $t$ used to represent the thickness of the inter-tow matrix is introduced in Figure 14. The same parameters are used to define the horizontal dimensions of the woven unit-cell geometry, as well as the bundle thickness and overall height of the unit-cell. Note that the thickness of the inter-tow matrix is truncated at the overall height of the unit-cell. This arises because the unit-cell is extracted from a multiple woven layer system.

The dimensioned views of Figure 15 illustrate the configuration of the void space and matrix material located in the gap region at the center of the woven unit-cell. In this figure the hole is taken to be circular, and centered in the middle of the unit-cell as shown in the top view. The section and gap region matrix views illustrate the shape of the matrix external to the tows and the hole used to develop the mathematical description of the matrix layer geometry containing a cylindrical hole. In real systems the hole cross-section may have an irregular shape which may be approximated by a square, circle or an ellipse. The upper and lower matrix layers are taken to be non-uniform with a variable thickness $t_m$. In the middle of the gap region the thickness of the matrix is zero, and at the peak of the interlace region the thickness may be truncated by the overall height $h$ of the woven ply. The expression for the thickness of the matrix layers is thus given by:

$$t_m(x,y) = \begin{cases} 0 & f(x,y) < \dfrac{g}{2} - t \\ \dfrac{1}{2} f(x,y) + t - \dfrac{g}{4} & \dfrac{g}{2} - t \le f(x,y) < \dfrac{g}{2} \\ t & \dfrac{g}{2} \le f(x,y) \end{cases} \tag{16}$$

where the spatial function $f(x,y)$ for a square, circular, and elliptical hole is given by

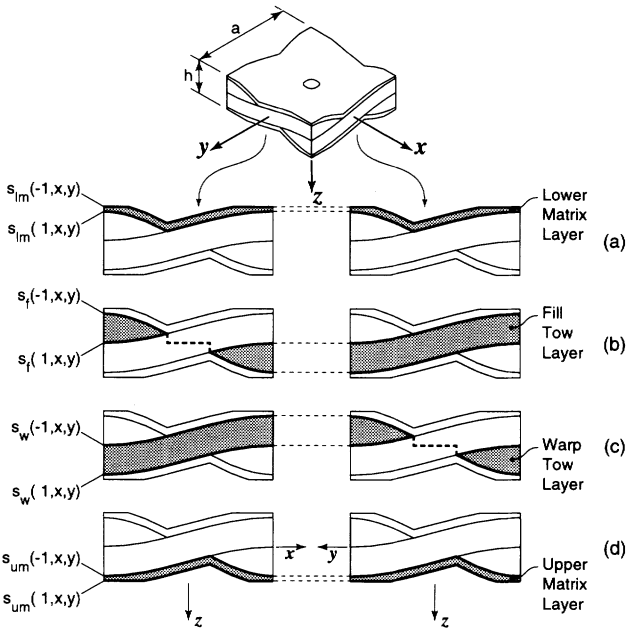


***Figure 13.*** *Side profiles of the four layers that constitute a single woven ply in the matrix layer model. The shaded portions in each row of figures illustrate two adjacent views of the (a) lower matrix layer, (b) fill tow layer, (c) warp tow layer and (d) upper matrix layer.*

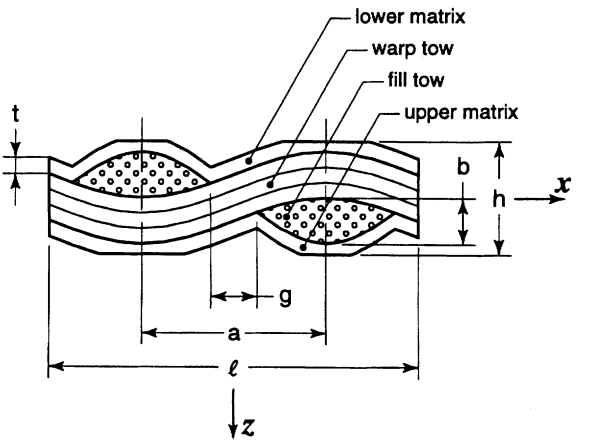


***Figure 14.*** *Geometric parameters used in the development of the matrix layer model.*

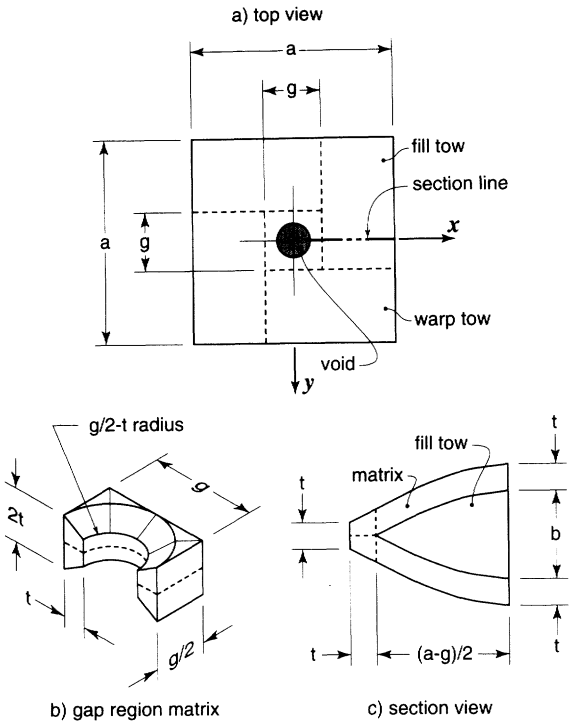


***Figure 15.*** *Detailed information about the structure of the model representing the matrix and void space in the matrix layer model: (a) top view of the symmetric unit-cell, (b) three-dimensional view of the structure of the matrix surrounding the void in the gap region and (c) section view giving the shape and dimensions of the matrix located in the gap region surrounding the void space.*

$$\text{square:} \quad f(x,y) = \text{MAX}(|x|, |y|)$$

$$\text{circle:} \quad f(x,y) = \sqrt{x^2 + y^2} \tag{17}$$

$$\text{ellipse:} \quad f(x,y) = \sqrt{(x/c)^2 + (y/d)^2}$$

The functions defining the top and bottom surfaces of the upper and lower matrix layers are then written in terms of the matrix/tow interface functions $s_m$ developed in the previous section and the above matrix layer thickness expression as

$$s_{lm}(\eta,x,y)=\begin{cases}\mathrm{MAX}\left(s_m(-1,x,y)-t_m(x,y),-\dfrac{h}{2}\right) & \eta=-1\\ s_m(-1,x,y) & \eta=+1\end{cases}\quad\text{(lower matrix)}$$

$$s_{um}(\eta,x,y)=\begin{cases}s_m(+1,x,y) & \eta=-1\\ \mathrm{MAX}\left(s_m(+1,x,y)+t_m(x,y),+\dfrac{h}{2}\right) & \eta=+1\end{cases}\quad\text{(upper matrix)}\qquad(18)$$

In order to validate the shape of the surface functions for the matrix layer model, Equations (12) and (18) were used to plot the surfaces of each of the four layers in Figure 16 for $b/a = 0.2$, $g/a = 0.286$, $h/a = 0.45$, and $t/a = 0.075$. While the fill tow and warp tow layers are identical to those of the porous matrix model shown in Figure 10, the upper and lower matrix layers are uniquely shaped to conform to the shape of the underlying bundles, as would be expected in composites fabricated by the chemical vapor infiltration technique. Equations (12) and (18) were also used to create the seven cross-sections of the matrix layer model repeating unit-cell, which are shown in Figure 17 for $b/a = 0.25$, $g/a = 0.25$, $h/a = 0.55$, and $t/a = 0.075$. As was the case for the porous matrix model, the tows are continuous in sections #1, #2, #6, and #7. In all of the cross-sections, the inter-tow matrix appears as a layer of thickness $t$ around the tows. In sections #1 and #7 the thickness of the ma-

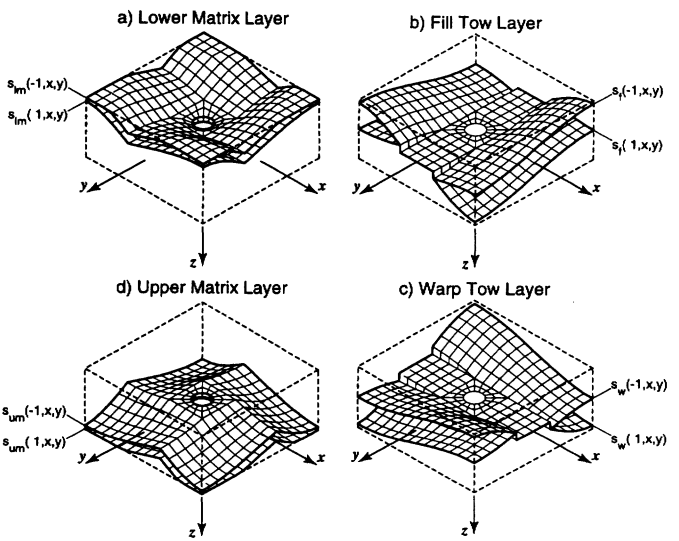


***Figure 16.*** *Surface plots of Equations (12) and (18) which correspond with the top and bottom surfaces of each layer within the matrix layer model.*

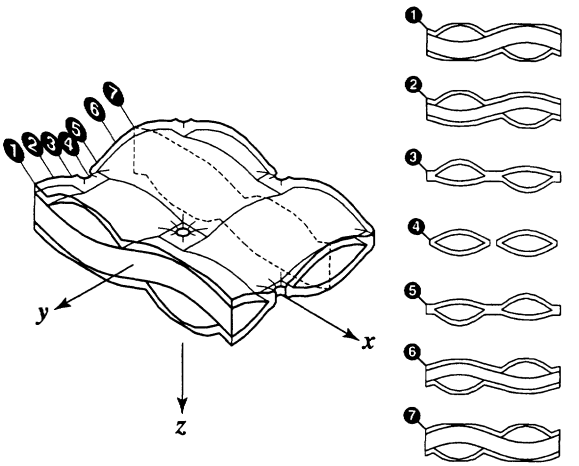


***Figure 17.*** *Layer matrix model cross-sectional views obtained using Equations (12) and (18). The cross-sections in the transverse direction are identical, and hence are not shown.*

trix is truncated at the peaks of the interlace regions as anticipated. Sections #3 and #5 are along the edge between the warp tow and the gap region, and at the same time do not pass through the hole at the center of the gap region. As such, the matrix appears to span the gap region, connecting the fill tows on either side. Section #4 does pass through the hole and illustrates a gap in the matrix as expected. As in the case of the porous matrix model, the cross-sections in the transverse direction are identical to those shown in Figure 17.

## 3. USE OF GEOMETRY FUNCTIONS IN THE MECHANICAL MODELING OF WOVEN COMPOSITES

The above approach to describing the unit-cell geometry can be used to simplify and extend existing analytical and numerical mechanics models of woven composites. In this section, the use of the proposed geometry functions in the development of mechanical models for woven composites is discussed. In particular, the incorporation of the proposed surface functions in the Modified Lamination Theory (see Reference [20]) as it relates to both porous matrix woven PMCs and layer matrix CVI CMC woven composites is first discussed. As discussed in Section 3.1 below, both unit-cell geometry models presented in this paper allow for the straight-forward implementation of the Modified Lamination Theory approach wherein the mid-plane strains and curvatures as well as force and moment resultants are taken to be functions of position $(x,y)$. Thus through the proposed surface functions, both unit-cell geometry modes treat the woven composite as a 4-layer laminate whose lamination morphology and layer thicknesses vary with position

$(x,y)$. Thus, spatially varying laminate stiffnesses that utilize in a straight-forward manner the surface functions presented in Section 2 above are proposed.

In Section 3.2, the geometric surface functions are integrated as needed to evaluate the matrix volume fractions as a function of the woven microstructure for the porous matrix and layer matrix geometry models. While enabling the reader to study the intricate interrelation between the relative volume fractions of the woven micro-constituents, this type of analysis also highlights, perhaps to a smaller but potentially significant degree, the efficiency of the ensuing mechanical model.

Finally, in Section 3.3, the unit-cell geometry functions are used to develop 3-D finite element meshes. We believe that this is an important step in the development of reliable mechanical models for woven composites. For example, analytical and finite element models reported in the literature are developed utilizing different approximations for the same woven unit-cell. As a result, the model predictions could not be compared directly to those obtained via the method of finite elements. As discussed in Section 3.3 below, 3-D finite element meshes are developed utilizing the same surface functions employed in the development of the spatially varying laminate stiffnesses presented in Section 3.1. This allows for the first time direct comparison of results obtained via the method of finite elements analytical mechanical models using the same woven unit-cell geometry characteristics.

### 3.1 Unit-Cell Geometry Functions and Spatially Varying Laminate Stiffnesses

As mentioned previously, the classical lamination theory presented by Jones [14] places no emphasis on laminates comprised of laminae with non-uniform thicknesses and positions. Several researchers have employed classical lamination theory to develop mechanics models of woven composite behavior [3,6,16,21]. The trend has been to subdivide the unit-cell into regions that resemble laminated composites with unidirectional layers of uniform thickness and position as an approximation. This approach has tended to result in lengthy and cumbersome expressions for the woven composite laminate stiffnesses [6]. However, if care is taken to ensure that the expressions properly account for the spatial variations, the classical lamination theory applies equally well to composites with non-uniform layers, as long as the basic deformation hypothesis is satisfied [22].

In Reference [23], the theory of plates for a composite laminate with highly non-uniform and disjointed layers was carefully developed. The purpose of the current paper is to present the details pertaining to surface expressions that may be used in such an analysis. However, in order to understand the utility of these functions we shall briefly present the resulting woven composite stiffnesses

presented in Reference [23]. The reader is referred to the above paper for the details of this mechanics model.

From the theory of plates for a composite laminate with non-uniform and disjoint layers employed in Reference [23], the spatially varying composite constitutive response is

$$\begin{Bmatrix} N_x \\ N_y \\ N_{xy} \\ M_x \\ M_y \\ M_{xy} \end{Bmatrix}(x,y) = \begin{bmatrix} A_{11} & A_{12} & A_{16} & B_{11} & B_{12} & B_{16} \\ A_{12} & A_{22} & A_{26} & B_{12} & B_{22} & B_{26} \\ A_{16} & A_{26} & A_{66} & B_{16} & B_{26} & B_{66} \\ B_{11} & B_{12} & B_{16} & D_{11} & D_{12} & D_{16} \\ B_{12} & B_{22} & B_{26} & D_{12} & D_{22} & D_{26} \\ B_{16} & B_{26} & B_{66} & D_{16} & D_{26} & D_{66} \end{bmatrix}(x,y) \begin{Bmatrix} \varepsilon_x^0 \\ \varepsilon_y^0 \\ \gamma_{xy}^0 \\ \kappa_x^0 \\ \kappa_y^0 \\ \kappa_{xy}^0 \end{Bmatrix}(x,y) \tag{19}$$

where $N_i$ and $M_i$, with $i = 1,2,3$ representing the normal/bending $x,y$, and shear/twisting $xy$ components, are the resultant forces and moments, respectively, acting at the mid-plane of the composite plate. The mid-plane strains are given by $\varepsilon_x^0$, $\varepsilon_y^0$, and $\gamma_{xy}^0$, and the mid-plane curvatures are $\kappa_x^0$, $\kappa_y^0$, and $\kappa_{xy}^0$. A more detailed definition of the quantities can be found elsewhere [23]. The composite stiffnesses for a fabric composite which may be reduced to a four layer system are

$$\begin{aligned} A_{ij} &= [s_{lm}^t - s_{lm}^b]\bar{Q}_{ij}^{lm} + [s_f^t - s_f^b]\bar{Q}_{ij}^{f} + [s_w^t - s_w^b]\bar{Q}_{ij}^{w} + [s_{um}^t - s_{um}^b]\bar{Q}_{ij}^{um} \\ B_{ij} &= \frac{1}{2}\{[(s_{lm}^t)^2 - (s_{lm}^b)^2]\bar{Q}_{ij}^{lm} + [(s_f^t)^2 - (s_f^b)^2]\bar{Q}_{ij}^{f} \\ &\quad + [(s_w^t)^2 - (s_w^b)^2]\bar{Q}_{ij}^{w} + [(s_{um}^t)^2 - (s_{um}^b)^2]\bar{Q}_{ij}^{um}\} \\ D_{ij} &= \frac{1}{3}\{[(s_{lm}^t)^3 - (s_{lm}^b)^3]\bar{Q}_{ij}^{lm} + [(s_f^t)^3 - (s_f^b)^3]\bar{Q}_{ij}^{f} \\ &\quad + [(s_w^t)^3 - (s_w^b)^3]\bar{Q}_{ij}^{w} + [(s_{um}^t)^3 - (s_{um}^b)^3]\bar{Q}_{ij}^{um}\} \end{aligned} \tag{20}$$

where the indices $i$ and $j$ take on the values 1, 2, and 6. The subscript notations $lm$, $um$, $f$, and $w$ denote the lower matrix, upper matrix, fill tow, and warp tow layers, respectively. The terms $\bar{Q}_{ij}^{k}$, with $k = lm, f, w, um$, represent the transformed local stiffnesses relating the microstresses and microstrains at a point in the plate. The functions $s_k^t$ and $s_k^b$, with $k = lm, f, w, um$, are the distances from the mid-plane of

the composite plate to the top and bottom surfaces of the respective layer. These surface functions may be abbreviated as

$$s_{lm}(\eta,x,y)=\begin{cases}s_{lm}^{b}(x,y) & \eta=-1\\ s_{lm}^{t}(x,y) & \eta=+1\end{cases} \qquad s_{f}(\eta,x,y)=\begin{cases}s_{f}^{b}(x,y) & \eta=-1\\ s_{f}^{t}(x,y) & \eta=+1\end{cases}$$

$$s_{um}(\eta,x,y)=\begin{cases}s_{um}^{b}(x,y) & \eta=-1\\ s_{um}^{t}(x,y) & \eta=+1\end{cases} \qquad s_{w}(\eta,x,y)=\begin{cases}s_{w}^{b}(x,y) & \eta=-1\\ s_{w}^{t}(x,y) & \eta=+1\end{cases} \tag{21}$$

where $\eta = +1$ denotes the top surface and $\eta = -1$ denotes the bottom surface. In the above equation, the functions $s_f(\eta, x, y)$, $s_w(\eta,x,y)$ and $s_{lm}(\eta, x, y)$, $s_{um}(\eta, x, y)$ are those given by Equations (12) and (15). Profiles of these functions are illustrated in Figure 7 for the plain weave architecture.

### 3.2 Volume Fractions Obtained Using the Unit Cell Geometry Functions

The geometry of the woven unit-cell gives rise to interesting trends in the tow and matrix volume fractions. The volume fraction occupied by the warp tow is $v_w = V_w / V_{tot}$ where the lower case $v$ is the dimensionless volume fraction, the upper case $V$ represents the actual dimensional volume, and the subscript *tot* denotes the total volume of the unit-cell. The volume occupied by the warp tow in the symmetric unit-cell is

$$V_w(x,y)=\int_{-a/2}^{a/2}\int_{-a/2}^{a/2}[s_w(+1,x,y)-s_w(-1,x,y)]\,dy\,dx \tag{22}$$

and the total volume of the unit-cell is $V_{tot} = ha^2$. For the balanced plain weave fabric with the overall unit-cell height $h$ equal to twice the tow height $b$, the total volume becomes $V_{tot} = 2ba^2$, and the volume fraction of warp tows after the coordinate transformation $\hat{x} = x/a$ and $\hat{y} = y/a$ is

$$v_w(x,y)=\int_{-1/2}^{1/2}\int_{-1/2}^{1/2}\frac{[s_w(+1,a\hat{x},a\hat{y})-s_w(-1,a\hat{x},a\hat{y})]}{2b}\,d\hat{y}d\hat{x} \tag{23}$$

Recall from Equation (10) that $s_{tow}$ [and hence $s_w$ from Equation (12)] is a linear

Recall from Equation (10) that $s_{tow}$ [and hence $s_w$ from Equation (12)] is a linear function of $b$. After substitution of Equations (10) and (12) into Equation (23), the $b$ parameter appears once in the numerator and denominator and can be canceled. As a result, the above equation is not a function of $b$ (hence $h$ for $h = 2b$), but does vary with changes in $g/a$. The volume fraction occupied by the fill tow in a balanced plain weave fabric is $v_f = v_w$, and the volume fraction of matrix material in the porous matrix model is $v_m = (1 - 2v_w)$. In Figure 18, the change in the matrix volume fraction of a balanced plain weave fabric with $h = 2b$ is monitored for $b/a = 0.15$, and $0 < g/a < 0.20$. Note that although a specific value of $b/a$ was chosen, the expression is independent of $b$ and the curve shown is identical for all $b/a$. The matrix volume fraction is shown to increase with increasing $g/a$ in Figure 18, as expected.

In the case of the matrix layer model, the volume fraction occupied by the tows is also independent of $b/a$ and is identical to that of the porous matrix model. The sum of the matrix and void volume fractions of the matrix layer model equals the matrix volume fraction of the porous matrix model. As such, the matrix volume fraction in the matrix layer model is a function of both $t/a$ and $b/a$ as well as $g/a$, and is computed by

$$v_m(x,y) = 2\int_{-1/2}^{1/2}\int_{-1/2}^{1/2} \frac{[s_{lm}(+1,a\hat{x},a\hat{y}) - s_{lm}(-1,a\hat{x},a\hat{y})]}{2b}\, d\hat{y}d\hat{x} \qquad (24)$$

noting that the volume occupied by the upper matrix is an anti-symmetric reflec-

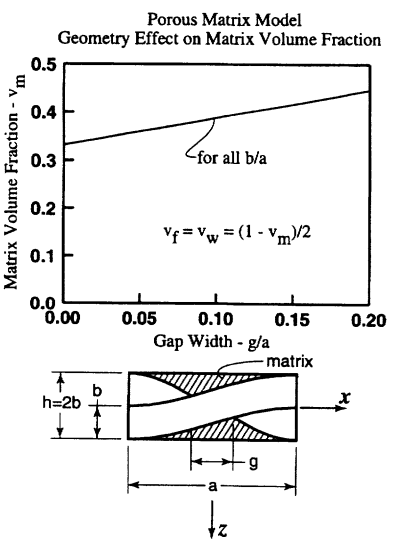


***Figure 18.*** *The inter-tow matrix volume fraction as a function of the woven unit-cell geometry parameter* g/a *for the porous matrix model.*

tion of that of the lower matrix. Further expansion of Equation (24) will not eliminate $b/a$ due to the inherent discontinuities of the $s_{lm}$ expression. Equation (24) is plotted in Figure 19 for $b/a = 0.15$, and three different values of $g/a$. The matrix volume fraction increases for *increasing* $t/a$. If $g/a$ is less than $2b/a$, then the center hole is filled with matrix material as $t/a \rightarrow b/a$, and the matrix volume fraction converges to that of the porous matrix model. The change in matrix volume fraction is monitored for changing $b/a$ at three different values of $g/a$ in Figure 20 for the matrix layer model. The thickness of the matrix layer is fixed at $t/a = 0.05$. In this case the actual volume occupied by the matrix remains constant, but the total volume of the unit-cell increases as $b/a$ increases, resulting in decreasing matrix volume fraction and increasing void volume fraction. As $b/a \rightarrow 0$ the matrix volume fraction reaches a plateau of different values for different $g/a$. This is because $t/a$ is fixed and for small $b/a$ is truncated by the overall height $h/a$ everywhere in the domain of the unit-cell, thus becoming identical to the porous matrix model.

### 3.3 Unit Cell Geometry Functions and 3-D Finite Element Meshing

An additional benefit of the geometry expressions presented above is their utility in developing numerical finite element models that match the geometry used for theoretical analysis. This yields the ability to conduct numerical comparisons directly with analytical solutions based on the same geometry models.

A finite element mesh of the plain weave unit-cell may be developed by employing Equation (12) to discretize and position nodes in the top and bottom surfaces of a single tow. Nodes located in the interior of the tows may be created by interpolating from the surface nodes, and the resulting regular array of nodes may be joined to form eight- or twenty-noded isoparametric brick elements. The resulting tow brick element mesh may be duplicated and rotated at 90° increments about the $z$ axis to form the remaining tows. In the process, care must be taken to ensure that the nodes at the interfaces of the tows are aligned, and coincident nodes must either be constrained to have the same displacements or removed. An example finite element mesh of the tows in the absence of matrix material consisting of 192 elements and 432 nodes is shown in Figure 21(a). The matrix material finite element meshes may be generated in a similar manner using Equation (15) in the case of the porous matrix model, and Equation (18) for the matrix layer model. Relatively course eight-noded finite element example meshes of the porous matrix and matrix layer model each consisting of 320 elements and 756 nodes are shown in Figure 21(b) and Figure 21(c), respectively. The appropriate material properties for each of the phases may be allowed to vary spatially and applied at the integration stations of each element.

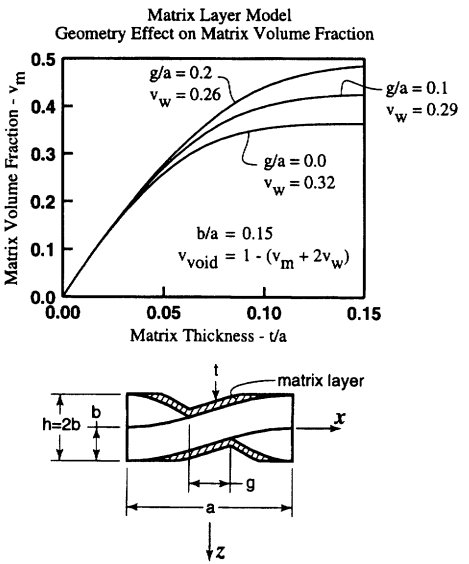


***Figure 19.*** *The inter-tow matrix volume fraction as a function of* t/a *and* g/a *for the matrix layer model. The matrix layer model is identical to the porous matrix model if* t/a > b/a *for* g/a < 2b/a.

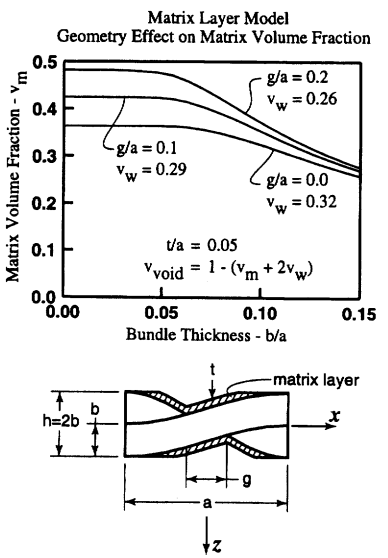


***Figure 20.*** *The inter-tow matrix volume fraction as a function of* b/a *and* g/a *for the matrix layer model. The matrix layer model is identical to the porous matrix model if* t/a > b/a *for* g/a < 2b/a.

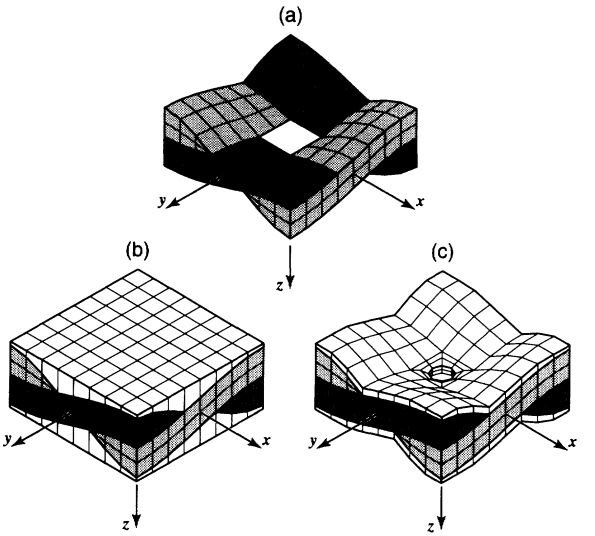


***Figure 21.*** *Finite element meshes generated using the surface functions with* b/a = *0.2,* g/a = *0.25,* h/a = *0.45, and* t/a = *0.05: (a) the woven tow meshes in the absence of the matrix, (b) the porous matrix model and (c) the matrix layer model.*

In addition to a three-dimensional brick element model, the geometry expressions presented herein could also be used to create a plate element model. In this case the unit-cell would be modeled with $N \times M$ grid of plate elements. The spatially varying local composite laminate stiffnesses in accordance with Equation (20) would be assigned to each integration station of each element. However, the 3-D finite element model will give greater insight to how well the Kirchhoff-Love deformation hypothesis is satisfied.

## 4. DISCUSSION

The approach of treating each component of the woven unit-cell as a single layer has greatly reduced the complexity involved with describing the geometry of the composite. Two variations of the plain weave architecture were studied and highly robust yet relatively simple geometry surface functions were developed. The more accurate and more compact expressions also reduce the complexity associated with further analysis of the unit-cell. In particular these surface functions are used in Reference [23] to develop series solutions for the unit-cell boundary value problems. Such problems would not be tractable using existing geometry models.

Each of the figures in this paper was created using the shape functions presented herein. As such, we can assess the effectiveness of this model by comparing the

three-dimensional surfaces with those presented elsewhere. In particular, Figure 5 illustrates a single tow as described by the surface functions presented herein. At the same time Figure 15 in Reference [12] illustrates a 3-D reconstruction of a single tow from data obtained experimentally. Here we note that there is a striking similarity between the two figures. While the experimental results show localized variations that do not appear in the present analytical model, the overall shapes are distinctly the same. The above local variations are expected to have a small impact on the overall mechanics of the woven composite material. In future work, the analytical and experimental models may be coupled by computing the geometry parameters statistically from the experimental data.

While the surface functions presented in this work are for a balanced plain weave fabric, they may be readily extended to apply to unbalanced hybrid composites with different $a$, $b$, and $g$ dimensions in the $x$ and $y$ directions. In addition the functions may be utilized to develop surface functions of more complex woven architectures via a sub-domain approach. The plain weave expressions represent the morphology of satin weaves in the undulating regions, outside of which the composite may be treated as a cross-ply laminate. The variation in the subregion morphology may be built into the surface functions in the same manner as presented in this work, yielding four expressions describing the geometry everywhere in the domain of the unit-cell. If this procedure is followed, then the local laminate constitutive relations of Equation (20) remain unchanged. Thus, the present work establishes in a fundamental manner the geometrical unit-cell characteristics of plain weave composites. As shown in complementary studies, this greatly facilitates the development of fundamental studies on the mechanical characteristics of these otherwise complex systems.

## 5. CONCLUSIONS

Continuous, simple to use surface functions have been developed for unit-cell woven geometries used in the modeling of polymer and ceramic matrix woven composites. The proposed functions are rather general and can be used in the reconstruction of a broad range of plain weave architectures. The Porous Matrix Model was developed to simulate the architecture often observed in plain weave PMCs. As such, the associated unit-cell geometry is fully occupied by the potentially porous phases of the fiber reinforced bundles and inter-bundle matrix material. On the other hand, the unit-cell geometry associated with CVI plain weave CMCs is known to exhibit large voids within the inter-bundle matrix phase. This feature was modeled using the Layer Matrix Model developed herein.

The woven unit-cell surface functions have been used to develop simple expressions for the spatially varying laminate stiffnesses employed by a Modi-

fied Lamination Theory scheme. Model efficiency resulting from the use of the same surface functions has been explored via volume fraction studies and via the development of robust 3-D finite element meshes. The development of this new class of woven unit-cell surface functions has been discussed within the broader context of the state-of-the-art mechanical modeling of woven composites. It is concluded, that this work establishes the theoretical foundation needed for the accurate description of complex woven geometries. As such, this work is expected to have significant impact on the development of computationally efficient, easy to use linear and non-linear mechanical models for woven composites.

## ACKNOWLEDGMENTS

Support for this work was provided by the National Science Foundation, Grant No. CMS94-96209.

## REFERENCES

1. T. Ishikawa and T.-W. Chou. 1983. "One-Dimensional Micromechanical Analysis of Woven Fabric Composites," *AIAA J.*, 21(12):1714–1721.
2. T. Ishikawa and T.-W. Chou. 1983. "In-Plane Thermal Expansion and Thermal Bending Coefficients of Fabric Composites," *J. Composite Mater.*, 17:92–104.
3. N. K. Naik and P. S. Shembekar. 1992. "Elastic Behavior of Woven Fabric Composites: I—Lamina Analysis," *J. Composite Mater.*, 26(15):2196–2225.
4. N. K. Naik and V. K. Ganesh. 1992. "Prediction of On-Axes Elastic Properties of Plain Weave Fabric Composites," *Composites Sci. & Tech.*, 45:135–152.
5. V. K. Ganesh and N. K. Naik. 1996. "Failure Behavior of Plain Weave Fabric Laminates under On-Axis Uniaxial Tensile Loading: I—Laminate Geometry," *J. Composite Mater.*, 30(16):1748–1778.
6. I. S. Raju and J. T. Wang. 1994. "Classical Laminate Theory Models for Woven Fabric Composites," *J. Composite Tech. & Res.*, 16(4):289–303.
7. A. Dasgupta and R. K. Agarwal. 1992. "Orthotropic Thermal Conductivity of Plain-Weave Fabric Composites Using a Homogenization Technique," *J. Composite Mater.*, 26(18):2736–2758.
8. A. Dasgupta and S. M. Bhandarkar. 1994. "Effective Thermomechanical Behavior of Plain-Weave Fabric-Reinforced Composites Using Homogenization Theory," *J. Engr. Mater. & Tech.*, 116:99–105.
9. J. D. Whitcomb. 1991. "Three-Dimensional Stress Analysis of Plain Weave Composites," in T. K. O'Brien (ed.), *Composite Materials: Fatigue and Fracture (Third Volume), ASTM STP 1110,* American Society for Testing and Materials, Philadelphia, pp. 417–438.
10. R. A. Naik. 1994. "Analysis of Woven and Braided Fabric Reinforced Composites," *NASA Contractor Report 194930.*
11. B. N. Cox and G. Flanagan. 1997. "Handbook of Analytical Methods for Textile Composites," *NASA Contractor Report 4750.*
12. S. W. Yurgartis, K. Morey and J. Jortner. 1993. "Measurement of Yarn Shape and Nesting in Plain-Weave Composites," *Composites Sci. & Tech.*, 46:39–50.
13. E. H. Glaessgen, C. M. Pastore, O. H. Griffin and A. Birger. 1996. "Geometrical and Finite Element Modelling of Textile Composites," *Composites Part B,* 27B(1):43–50.
14. R. M. Jones. 1975. *Mechanics of Composite Materials.* Hemisphere Publishing Corp.

15. J. L. Kuhn and P. G. Charalambides. 1998. "Elastic Response of Porous Matrix Plain Weave Fabric Composites: Part I—Modeling," *J. Composite Mater.*, 32(16):1426–1471.
16. P. S. Shembekar and N. K. Naik. 1992. "Elastic Behavior of Woven Fabric Composites: II—Laminate Analysis," *J. Composite Mater.*, 26(15):2226–2246.
17. W.-S. Kuo and T.-W. Chou. 1995. "Elastic Response and Effect of Transverse Cracking in Woven Fabric Brittle Matrix Composites," *J. Amer. Ceram. Soc.*, 78(3):783–792.
18. E. Inghels and J. Lamon. 1991. "An Approach to the Mechanical Behaviour of SiC/SiC Ceramic Matrix Composites: Part I—Experimental Results," *J. Mater. Sci.*, 26:5403–5410.
19. X. Aubard. 1995. "Modelling of the Mechanical Behaviour of a 2-D SiC-SiC Composite at a Meso-Scale," *Composites Sci. & Tech.*, 54:371–378.
20. J. L. Kuhn and P. G. Charalambides. 1998. "Elastic Response of Porous Matrix Plain Weave Fabric Composites: Part II—Results," *J. Composite Mater.*, 32(16):1472–1507.
21. K. R. Vaidyanathan, A. D. Kelkar and J. Sankar. 1993. "Prediction of Elastic Properties of Ceramic Matrix Composites Using a Plain Weave Classical Laminate Theory," *Ceram. Engr. Sci. Proc.*, 14(9-10):1066–1076.
22. J. L. Kuhn and P. G. Charalambides. 1997. "On the Accuracy of Approximate Elastic Micro-Fields in Plain Weave Fabric Composites under In-Plane Loading," submitted to *J. Composite Mater.*, November.
23. J. L. Kuhn, S. I. Haan and P. G. Charalambides. 1998. "A Semi-Analytical Method for the Calculation of the Elastic Micro-Fields in Plain Weave Fabric Composites Subjected to In-Plane Loading," submitted to *J. Composite Mater.*, in press.